

## SECONDARY FLOWS AND TURBULENCE FOR STAGGERED AND NON-STAGGERED ELECTRODE EMITTERS

NIELS F. NIELSEN<sup>1</sup>, POUL S. LARSEN<sup>2</sup> AND CHRISTER  
LÖFSTRÖM<sup>1</sup>

<sup>1</sup>FLSmidth Airtech, Ramsingsvej 30, DK-2500 Valby, Denmark  
(nfn@flsairtech.com)

<sup>2</sup>Department of Mechanical Engineering, Fluid Mechanics Section,  
Technical University of Denmark, Building 403, DK-2800 Kgs. Lyngby, Denmark

### ABSTRACT

Simulation models for sizing ElectroStatic Precipitators (ESPs) have been presented for the last 15 to 20 years. But still today the majority of the models are two-dimensional or semi-two-dimensional. Such restrictions exclude the possibility for investigating the influence of the physically important secondary flows ('ion winds') induced by the electric field. Secondary flows aid or oppose particle motion towards the collecting plates which along with turbulent diffusion play an important role in the resulting computed particle emission from a given ESP. But secondary flows are also found to determine the level of turbulence, which affects directly the coefficient of turbulent diffusion since this is often assumed to be proportional to the eddy diffusivity of momentum exemplified by the  $k,\epsilon$ -model.

Experimental results obtained in a 0.2x0.2 m by 1.0 m long, seven-electrode laboratory scale model ESP at low particle load are used to first verify the reliability of the present CFD-model for staggered and non-staggered electrode emitters, in terms of current-voltage-characteristics, current density at collecting plate, turbulence level, and strength of secondary flows. Then parameter studies illustrate how the level of turbulence and the pattern and strength of secondary flow change, both along the ESP for fixed current and at the downstream station for increasing current. The distribution and magnitude of the turbulent diffusivity as well as computed efficiency are discussed.

## INTRODUCTION

Numerical modelling of the precipitation process is challenging and many approaches have been made to model ElectroStatic Precipitators (ESPs) (Anagnostopoulos & Bergeles, 2002, Arrondel et al., 2001, Egli et al., 1996, Gallimberti, 2004, Houlgreave et al., 1996, Lawless, 1996, Lind et al., 2004, Medlin et al., 1998, Meroth et al., 1996, Parasram & Taylor, 2001, Schmid & Buggisch, 1998, Schmitz et al., 2001, Soldati, 2003, Zamany, 1992, 1995a). The literature contains models with different complexity but many are two-dimensional, hence unable to predict the complex electro-hydrodynamic flows that are likely to appear in most industrial designs. The motivation for improved model development is the need to ensure confidence in predicting the efficiency of existing and modified ESP designs, e.g. through modified emission electrodes.

In the negative, fixed-point corona precipitator, the non-uniform electrostatic field and the induced charge density of gas ions give rise to a complex three-dimensional, body force field acting on the charged gas flow. As a result the incoming uniform bulk flow gets distorted as secondary flows in the form of axial rolls develop and turbulence is generated (Thomsen et al. 1982, Davidson and Shaughnessy 1986, Zamany 1992). The efficiency of the precipitator is impaired, in part by increasing turbulence levels, as shown in a theoretical study by Leonard et al. (1980), and in part by organised secondary flows, as shown by Larsen and Sorensen (1984). The development of secondary flows in barbed-wire, negative corona ESP's has been studied theoretically by a simple integral model (Larsen 1986) and in more detail (determining also the nature and strength of the flows) by including the charging history of individual particles (Blanchard et al. 2001). Detailed experimental results on both turbulence levels and secondary flow strength and structures have been obtained by stereo-PIV (Ullum, et al. 2004, Ullum and Larsen 2004, Larsen et al. 2004).

The present experimental and numerical study concerns the local scale problems in a negative corona, barbed-wire, smooth-plate electrostatic precipitator. The results include comparison between experimental and computational data. Focus is on staggered and non-staggered electrode emitters because it remains to ascertain how these electrodes affect secondary flows, turbulence and particle diffusivity, which in turn affect the ESP efficiency.

## EXPERIMENTAL SET-UP

The 200×200 mm by 1000 mm long test section (Figure 1) has 2 grounded aluminum sides that serve as collector plates, and 2 glass sidewalls that support 7 discharge electrodes, starting at  $x = 200$  mm from the inlet, spaced 100 mm apart.

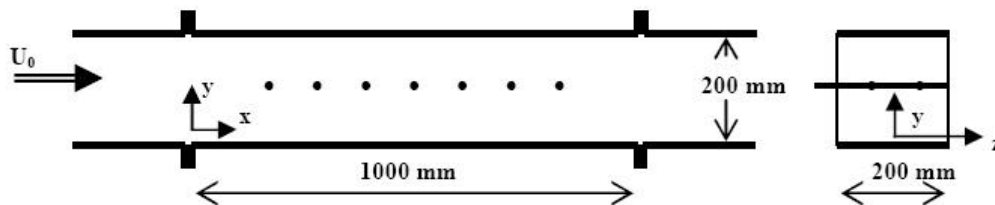


Figure 1. Side view and cross section of 1000x200x200 mm laboratory scale model ESP with 7 electrodes spaced 100 mm apart, located at  $x = 200, 300, 400, \dots 800$  mm.

For easy optical access, the square test section is oriented so that electrodes and collector plates are horizontal rather than vertical. The effect of gravity on particles is negligible, however, since the terminal velocity would be less than 0.3 mm/s for a size range of 1-3  $\mu\text{m}$  of interest. Electrodes are connected to a low-ripple, high voltage, DC-power supply (Hypotronics, model 800PL).

Two types of electrode emitters were studied (Table 1 and Figure 2) that of a non-staggered and that of a staggered emitter arrangement. Both electrodes giving rise to some spanwise and axial periodicity in the induced electrical field.

Electrode type	body diam. (mm)	emitter diam./length (mm)	no. of corona points	emitter spacing along electrode and orientation relative to axial
CA-100-100	3	1.0 / 5.0	4	100 mm non-staggered, $\pm 0^\circ$ (pointing axially)
CA-100S-100	3	1.0 / 5.0	3	100 mm staggered, $\pm 0^\circ$ (pointing axially)

Table 1. Types of electrodes investigated. Non-staggered and staggered.

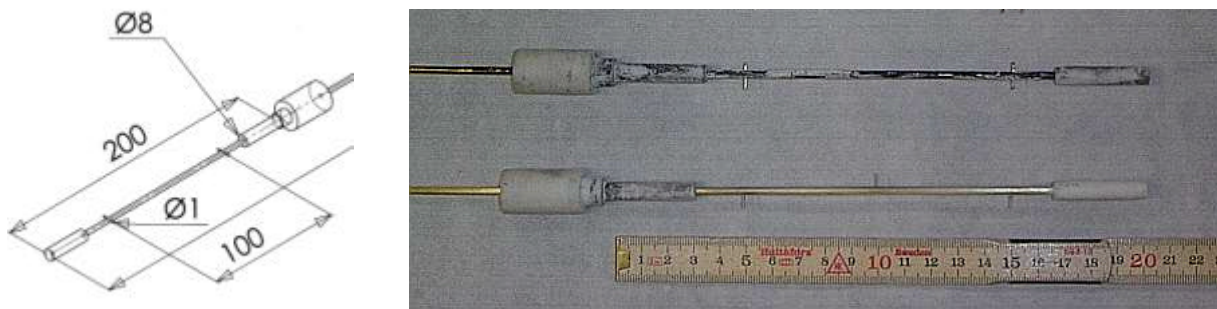


Figure 2. Two types of electrodes: CA-100-100 non-staggered (left and upper right) and CA-100S-100 staggered (lower right).

Upstream of the test section there is a 16:1 contraction and an 800×800 mm calming section with screens, upstream of which – in a 100 mm diameter inlet nozzle – solid Rollovit particles ( $> 98\%$   $\text{CaCO}_3$ ,  $< 0.35\%$   $\text{SiO}_2$ , density 2700  $\text{kg/m}^3$ , refractive index 1.68, relative permittivity  $\epsilon_r = 8.6$ , resistivity  $> 10^{10}$   $\Omega\text{-cm}$ ) are fed into the flow at a low concentration of about 0.1  $\text{g/m}^3$  by a rotating brush on the top of a piston-cylinder arrangement. The mean particle diameter was measured to about 1.86  $\mu\text{m}$ . All experiments were conducted at room temperature. Note that the mean particle diameter is relatively small and that the resistivity is relatively low.

Bulk flow mean velocity  $U_0$  was measured by a standard orifice-plate flow meter, the pressure drop being read from a precision micro-manometer. Voltage and total current to electrodes were read from instruments integrated into the high-voltage power supply.

Three-component velocity data (u,v,w) for spatially resolved fields at various y,z-planes along the test section were obtained with a digital stereo PIV system, see Larsen et al. (2004) for details which include experimental accuracy. The velocity data covered the flow area  $z \in [-48.1, 92.8]$  mm by  $y \in [12.7, 98.6]$  mm, corresponding to more than half of the lower half of the cross section and

yielding the three components of 51×52 instantaneous velocity vectors. Regions near walls could not be resolved because of optical problems associated with reflections and scattered light.

### NUMERICAL MODEL

In the present study the numerical model solves the three-dimensional electrical and turbulent flow field and concentration of a number of different particle classes. The most important interactions between the different fields are included in the model and sketched by the arrows in Figure 3. The electrical force is the main mechanism in the precipitator process and the three-dimensional model of Zamany (1992) is used to calculate the electrical conditions influenced by ionic and particle space charge. This model solves simultaneously the coupled electric and current density fields. The electric field takes into account the influence of ionic convection and diffusion due to corona discharge, the presence of particle space charge (electric field distortion) and the effect of dust resistivity at the collector plates. The weak interaction from the flow field on the electric field, i.e. the current due to convection of charge, is not included. However, the strong interaction of the electrical field (body force) on the flow field as well as the actual geometry is taken into account as seen from the induced secondary flows. The weak interaction from the particle field on the flow field is not included. The turbulent particle transport controlled by both electric field (including particle charging) and flow field (fluid particle dynamics) is modelled by an Eulerian approach due to the highly coupled problem, i.e. by treating particles as a second continuum phase characterized by its concentration, which also reduces the computational effort.

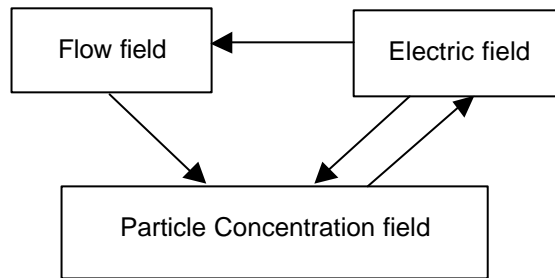


Figure 3. Interaction between different components of the ESP simulation model.

### Model Description

The three-dimensional electrostatic field between discharge electrode and collector plate in terms of potential and charge density is computed by solving

$$\tilde{\mathbf{N}} \cdot \mathbf{E} = (\rho_i + \rho_p) / \epsilon_0, \quad \tilde{\mathbf{N}} \cdot \mathbf{J} = 0, \quad \text{where} \quad \mathbf{J} = (\rho_i b_i \mathbf{E} - D_i \tilde{\mathbf{N}} \rho_i) + (\rho_p b_p \mathbf{E} - D_p \tilde{\mathbf{N}} \rho_p). \quad (1)$$

$\mathbf{E} = -\tilde{\mathbf{N}} \phi$  is the electric field,  $\phi$  the electric potential,  $\rho_i$  and  $\rho_p$  the space charge density of gas ions and particles, respectively,  $\epsilon_0$  the electric permittivity,  $\mathbf{J}$  the current density,  $b_i$  and  $b_p$  the mobility of gas ions and particles, respectively, and  $D_i$  and  $D_p$  ion and particle diffusivity coefficients, respectively. For further details of modelling procedure and coefficient values, see Zamany (1992, 1995a, 1995b) and Akoh and Nielsen (2000).

The three-dimensional turbulent gas flow field is computed within the environment of the commercial CFD code STAR-CD. The flow field is governed by the Navier-Stokes equations, which are solved together with the equation of mass conservation. Turbulence is modelled by the standard k- $\epsilon$  model (Launder & Spalding, 1974), which is widely used for industrial internal flows and comprises

differential transport equations for the turbulent kinetic energy  $k$  and its dissipation rate  $\epsilon$ . The high Reynolds number form is used in conjunction with the so-called “law of the wall”. This choice is based on the best compromise between accuracy and boundary layer resolution. The body force from the influence of the electric field,  $\mathbf{F}_e = \rho_i \mathbf{E}$ , is added as source terms in the momentum equations. For further details of modelling the turbulent flow field, see Ferziger & Peric (1996), STAR-CD manual (2002), and Wilcox (1993).

The concentration field (particle motion) is computed within the STAR-CD environment as an Euler formulation. The particles are divided into  $d_i$  classes each having concentration  $c_i$  ( $n_i$  scalar equations). The transport equation for  $c_i$  includes influence from the electric field by a source terms  $-\tilde{\mathbf{N}} \cdot (c_i \mathbf{v}_e)$ ,  $\mathbf{v}_e$  denoting the electric drift velocity. The influence from the flow field is included in the particle drift velocity,  $\mathbf{v}_p = \mathbf{v}_f + \mathbf{v}_e$ ,  $\mathbf{v}_f$  denoting the gas flow velocity. The particle mass flux deposited on the collecting plates is calculated as  $\Delta \dot{m}_{\text{dust}} = \int_A \mathbf{v}_p c \cdot \mathbf{n} dA$ , where  $\mathbf{n}$  is the outward normal to the cell flux area  $A$ . Turbulent transport employed the diffusion approximation, using diffusivity  $D_T = \nu_T / \sigma$ , where  $\nu_T = C_\mu k^2 / \epsilon$  denotes the eddy-diffusivity of momentum from the  $k, \epsilon$ -model of the velocity field, and  $\sigma$  ( $= 0.9$ ) is the turbulent Prandtl-Schmidt number having the same value for all particle classes.

### Geometry, computational mesh and boundary conditions

The ESP geometry of the present study is shown in Figure 4. The figure shows one field with a set of parallel collecting plates and a series of electrodes. The flow is from left to right (axial flow between parallel collecting plates). The simulation model is based on a cell model for the electric field and a section model for the flow and concentration fields. Thus, based on the strategy of Zamany (1992) the electric field is solved on the unit cell geometry.

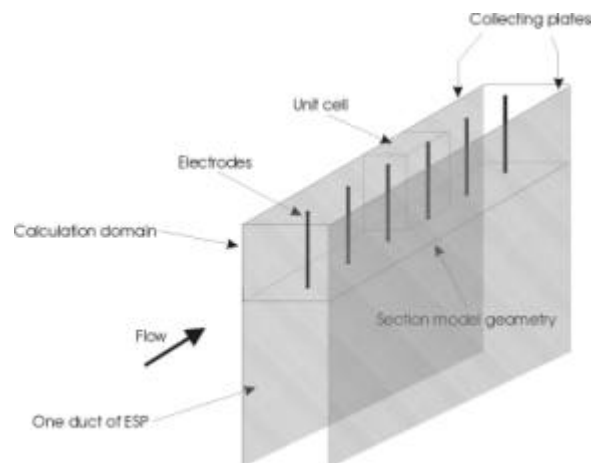


Figure 4. Computational domain with electrodes.

The unit cell is defined as a small symmetrical calculation volume between two electrodes in the axial direction and between one collector plate and the electrode symmetry line in the transversal direction (see Figure 4). The flow field and the particle concentration field are solved on the section model geometry due to the elliptic nature of the three-dimensional flow field. The section model is defined

as the calculation domain represented by the length of one electrical field in the axial direction and as the distance between one collector plate and the electrode symmetry line in the transversal direction (i.e. several unit cells). The height of the unit cell as well as of the section model is arbitrary and depends on the distance between the emitters of the electrodes. The unit cell/section model strategy requires interpolation of the electrostatic field to the flow field and particle concentration field (unit cell to section model geometry).

The computational mesh consists of a Cartesian mesh structure with cubic cells of any size. The local mesh refinement option in STAR-CD is not included and the actual geometry of the electrodes is not modelled flow-wise, but only electrically.

The boundary conditions for the electric field are:  $\partial/\partial n = 0$  at symmetry planes (electrodes center line and cell top and bottom),  $\phi = 0$  and  $\rho_i = 0$  at the collector plate,  $\phi = \phi_0$  at the electrode, and  $\rho_i = \rho_0$  at corona points, the latter being adjusted iteratively until the calculated mean current density  $J_m$  at the collector plate equals the wanted value for the specified electrode potential  $\phi_0$  (Zamany, 1995a). The boundary conditions of the section model for the flow field are:  $\partial/\partial n = 0$  at symmetry planes, no-slip at the collector plate, a uniform velocity profile at the inlet, and exit mass flow fixed from overall continuity considerations. The boundary conditions of the section model for the particle concentration field are: uniform concentration at inlet,  $\partial/\partial n = 0$  at the outlet, at collector plate (zero slope), and at symmetry lines (zero flux).

Modelling of ESPs is usually done at two levels. Globally, focus is on the gas flow and its distribution over width and height of a complete ESP-unit (Nielsen et al. 2004). Locally, focus is on the electrostatic field, gas flow and particle motion and precipitation, as well as possibly the mechanical operations like rapping.

The purpose of the present study is accurate local modelling of the precipitation process in a laboratory model of an ESP with two different electrode emitter-geometries and low particle loading, ignoring rapping etc.

## RESULTS AND DISCUSSIONS

Five elements related to the basic understanding of ESP modelling have been considered in the presentation of results. First, some model verification by comparing experimental data with computed data; second, a parametric study of the axial development of turbulence and secondary flow; third, a parametric study of the downstream developed state of turbulence and secondary flow for increasing current density; then, a study of the particle diffusivity coefficient which is a key in ESP modelling; and finally, some parametric effect on the computed efficiency. For all cases, results of non-staggered and staggered electrode emitters are presented and interpreted. Also, the separate effect of secondary flows, for example on turbulence level, has been studied by repeating a given calculation while setting to zero the electric body force acting on the gas.

Dimensional analysis shows two dimensionless groups for the dynamics of the flow, the usual Reynolds number,  $Re = U_b l_y / \nu$ , which is of secondary importance, and the electro-hydrodynamic modulus

$$N_{EHD} = (J_m / b_i) l_y / (1/2 \rho U_0^2) , \quad (2)$$

being the ratio of transverse electric force to axial flow inertia, similar to an inverse Froude modulus.  $J_m$  denotes the mean current density,  $b_i$  the mobility of gas ions ( $= 2.1 \times 10^{-4} \text{ m}^2/\text{Vs}$  for air at room temperature),  $\ell_y$  ( $= 0.1 \text{ m}$ ) the electrode to collector plate distance,  $\rho$  ( $= 1.2 \text{ kg/m}^3$ ) the gas density, and  $U_0$  the bulk velocity. In addition to the geometry of electrodes and location of corona discharge points the parameter (2) has been found to be useful in correlating parameters such as turbulence level (Yamamoto and Velkoff 1981, Ullum et al 2004).

For a simple description of the velocity field and the particle concentration field, averaged over the cross section at any axial position, we may think of four parameters: the bulk velocity  $U_0 = \langle U \rangle_{yz}$ , the turbulence intensity  $\langle Tu \rangle_{yz} = (2\langle k \rangle_{yz}/3)^{1/2}/U_0$  calculated from turbulent kinetic energy  $k_{yz} = \frac{1}{2} \langle u_k u_k \rangle_{yz}$ , and bulk velocity, the strength of secondary flow represented by the mean value of magnitude of the velocity vector  $\langle (V,W) \rangle_{yz}$ , and the turbulent viscosity normalized with the kinematic viscosity  $\langle \nu_T/\nu \rangle_{yz}$ . Note that  $\langle \nu_T/\nu \rangle_{yz}$  values in numerical models serve to determine the turbulent diffusivity  $D_T$  of particles hence are crucial for calculating concentration distributions and efficiency. All parameters described show local variations over the cross section, as seen below.

### Experimental verification

Figure 5 shows the good agreement between measured and computed current-voltage characteristics (CVCs) in terms of mean current density  $J_m$  versus electrode potential  $\phi_0$  for the non-staggered and staggered electrode emitters of Table 1. Note that although the CVC's for non-staggered and staggered electrodes are quite similar they may still have different current density at the collecting plate. This is demonstrated in Figures 6 and 7 showing both computed current density distributions at collector plate for non-staggered and staggered electrode emitters and observed dust patterns (photos from scale model).

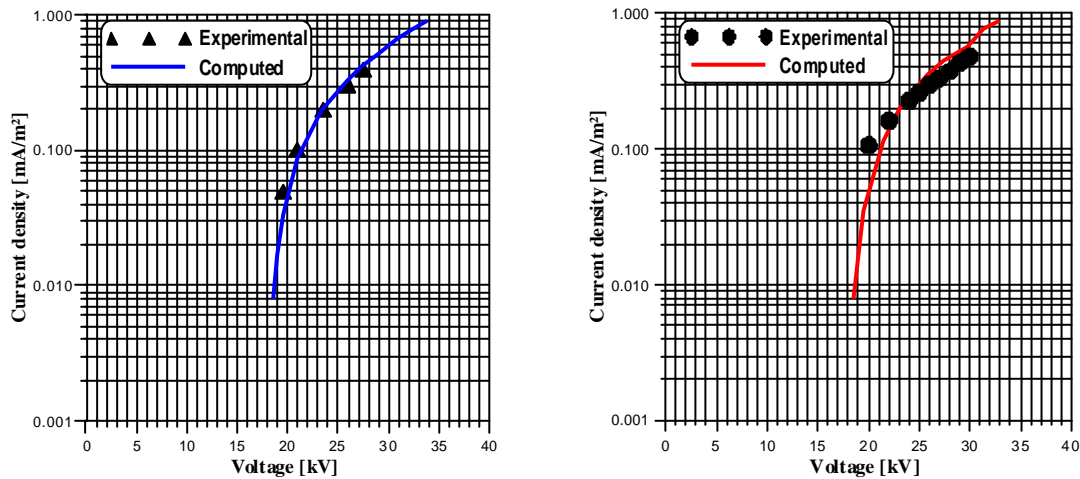


Figure 5. Measured and computed Current-Voltage Characteristics (CVC's) for CA-100-100 (left) and CA-100S-100 (right) electrode emitters.

As expected the current density at the collecting plates are different for non-staggered and staggered electrodes (Figure 6, left). One electrode quality criterion is the ratio between the area with current density below a certain limit, say  $280 \mu\text{A/m}^2$ , and the total collecting area. Another criterion is the ratio between maximum current density and mean current density. The calculated values for non-staggered and staggered electrodes are 34% and 34%, respectively, for the area ratio and 2.44 and

2.38, respectively, for the current density ratio. Hence based on these evaluation criteria the two electrodes investigated are equally good (case of  $N_{EHD}=0.333$ ).

Comparing the computed current density at the collector plates with the observed dust pattern at the lower collector plate clearly shows similar patterns. Regions of compacted dust (white areas) correspond to high current density and regions with uncompacted dust (darker dendritic areas) correspond to low current density. This fact is accentuated in Figure 7 where the collector plate has been cleaned with shop air leaving no dust in regions with computed current density lower than  $280 \mu\text{A}/\text{m}^2$  (highlighted with green colour). The observed dust structure of the different regions was found to be in agreement with those described by Blanchard et al. (2002). In conclusion there is a clear relationship between current density at collector plates and areas of compacted and uncompacted dust. Hence computed current density patterns may identify regions of high risk of re-entrainment.

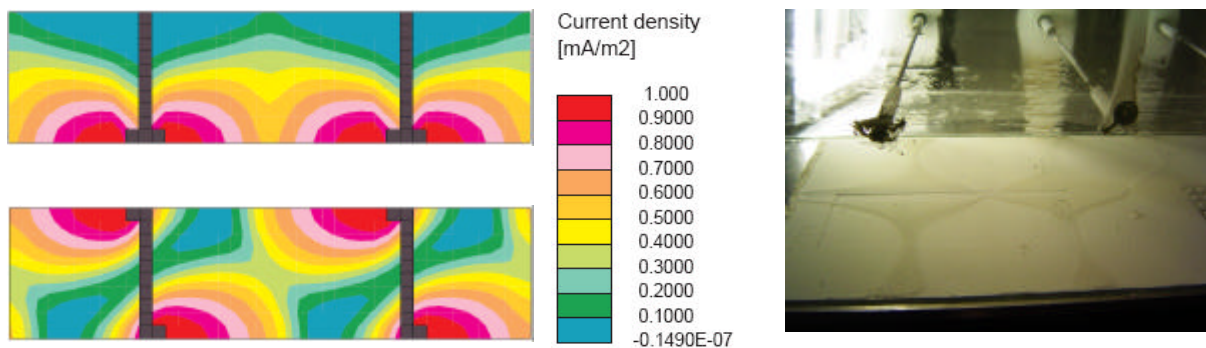


Figure 6. Computed values of current density distribution at collector plate for non-staggered (upper left) and staggered (lower left) electrode emitters and photo in scale model of observed dust pattern at lower collector plate for non staggered electrode (right). Axial position: between 1<sup>th</sup> and 2<sup>nd</sup> electrode. Inverse electric Frode number is  $N_{EHD}=0.333$ .

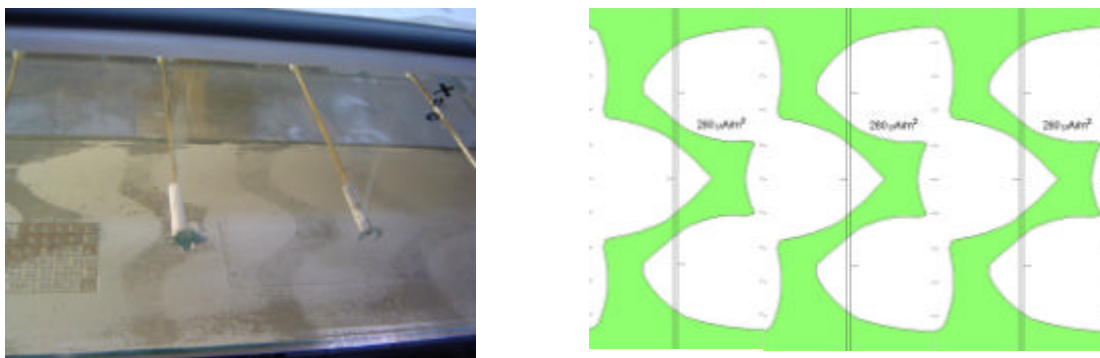


Figure 7. Left: Photo in scale model of dust pattern at lower collector plate after cleaning with shop air for staggered electrode emitters. Right: Computed current density at collector plate with regions below  $280 \mu\text{A}/\text{m}^2$  coloured. Axial position: between 3<sup>rd</sup> and 4<sup>th</sup> electrode. Inverse electric Frode number is  $N_{EHD}=0.333$ .

Note that it is crucial for the reliability of ESP-models that computed CVC's and distributions of current density be verified experimentally before proceeding to other results.

Figure 8 shows measured and computed mean turbulence intensity,  $\langle Tu \rangle_{yz}$ , and mean strength of secondary flow,  $\langle (V,W) \rangle_{yz}$ , versus  $N_{EHD}$  for non-staggered and staggered electrode emitters. Computed  $\langle Tu \rangle_{yz}$  fits very well with measured data. In general increasing

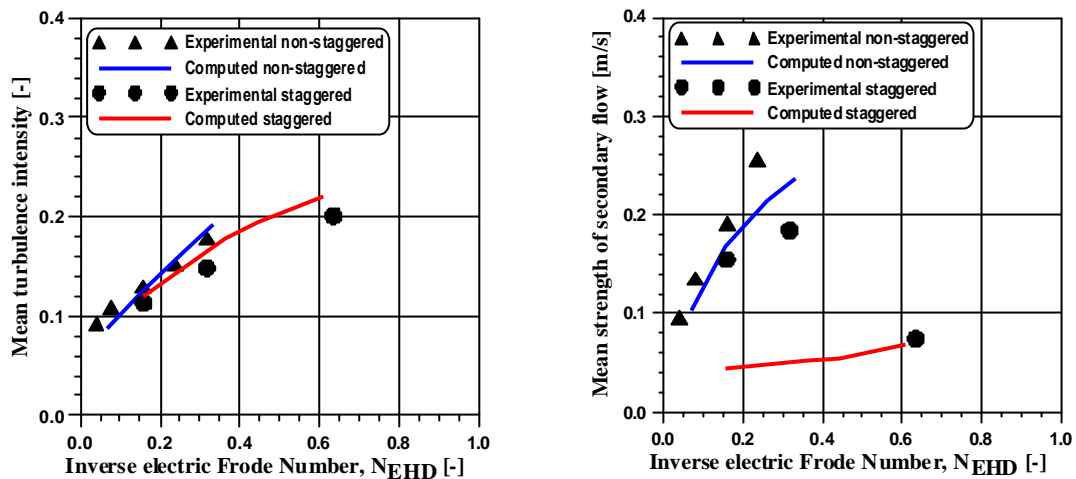


Figure 8. Measured and computed values of mean turbulence intensity (left) and magnitude of mean secondary flow (right) versus inverse electric Frode number for staggered and non-staggered electrode emitters. Axial position: mid between 6<sup>th</sup> and 7<sup>th</sup> electrode.

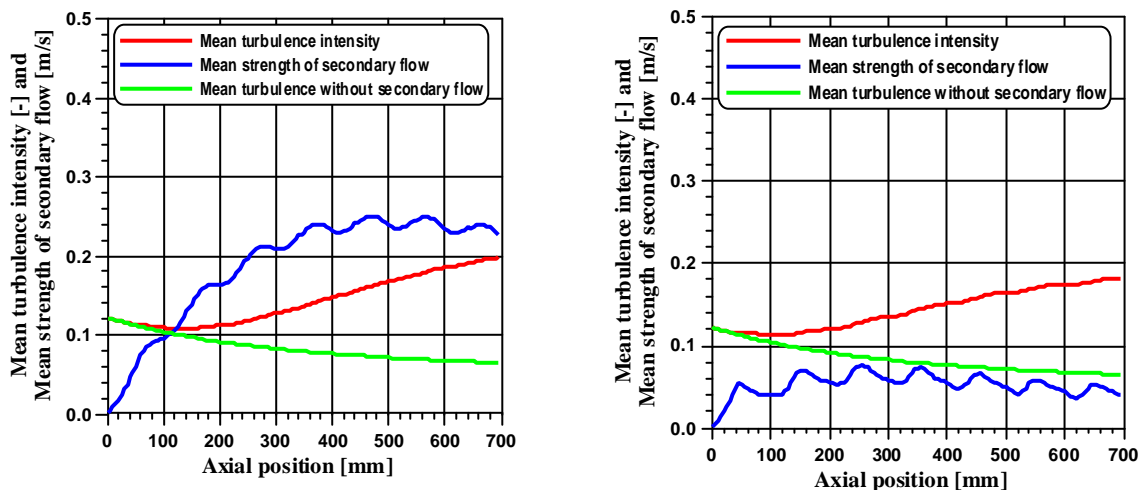


Figure 9. Computed values of mean turbulence intensity and magnitude of mean secondary flow versus axial position for non-staggered (left) and staggered (right) electrode emitters. Case without secondary flow included. Inverse electric Frode number is  $N_{EHD}=0.333$ .

values are found for increasing  $N_{EHD}$  with slightly higher values for the non-staggered electrode. Computed  $\langle (V,W) \rangle_{yz}$  for the non-staggered electrode shows good agreement with measured data, but for the staggered electrode considerable scatter is observed. This difference is explained by

noting the expected aspect ratio of rolls of secondary flow driven by the ‘ion wind’, being 100/50 and 100/25 for non-staggered and staggered electrodes, respectively. Rolls of the high 4:1 aspect ratio are likely to be more weak and/or unstable (see computed vector fields in Figure 10).

### **Turbulence level and secondary flow – Axial development**

Figure 9 shows computed axial variation of  $\langle Tu \rangle_{yz}$  and  $\langle VW \rangle_{yz}$  between inlet and outlet of the laboratory model for the non-staggered and the staggered electrode emitters at  $N_{EHD}=0.333$ . The cross-sectional average of turbulence intensity, after a slight decrease at the

inlet, increases almost linearly to a maximum value at the outlet of 20% and 18% for non-staggered and staggered electrodes, respectively. For comparison, setting the electric body force acting on the gas to zero (no secondary flow), the turbulence intensity continues to decrease downstream. This shows that the turbulence level in ESP’s is produced by the secondary flows, which must be included in a computational model that should therefore be fully three-dimensional.

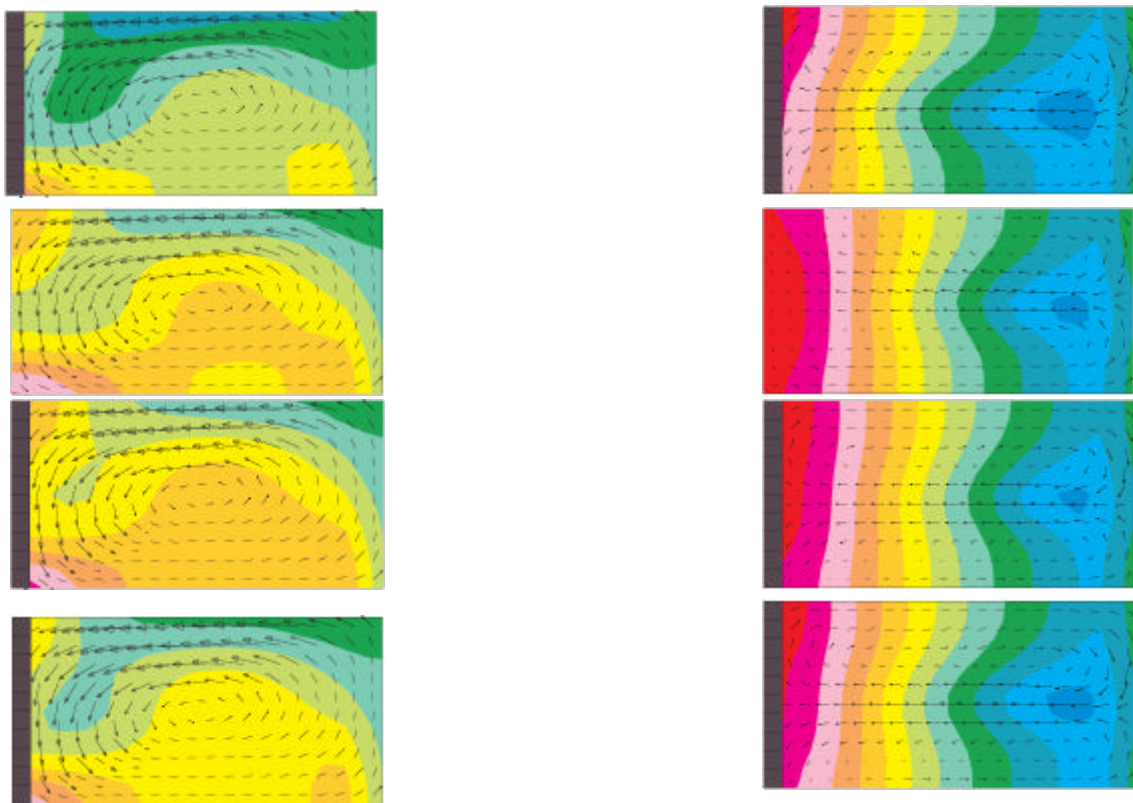


*Figure 10. Computed turbulence intensity (contours) and secondary flow (vectors) between 5<sup>th</sup> and 7<sup>th</sup> electrode for non-staggered (left) and staggered (right) electrode emitters. Inverse electric Frode number is  $N_{EHD}=0.333$ .*

The strength of secondary flow increases to a maximum value at the 5<sup>th</sup> electrode, showing a slight decrease downstream of this position for the non-staggered electrode (Figure 9). In the case of the staggered electrode the maximum strength of secondary flows is reached much faster and it is noted

that in general the strength of secondary flow for the staggered electrode is much lower than the non-staggered electrode. It appears that the local maximum strength of secondary flow is obtained just downstream of each electrode probably due to the strong local ‘ion wind’ near corona points.

Figure 10 shows contours of turbulence intensity and superposed vector maps of secondary flows for the axial variation between 5<sup>th</sup> and 7<sup>th</sup> electrode for non-staggered and staggered emitters at  $N_{EHD}=0.333$ . Throughout, the turbulence intensity distribution is developing for the non-staggered electrode while no development of pattern is seen for the staggered electrode, but still an increasing mean value as shown in Figure 9. Velocity vectors show well organized rolls in both cases but with the notable difference that the staggered electrode has twice as many rolls (twice the aspect ratio) as the non-staggered electrode.

### Turbulence level and secondary flow – Increasing current density

Figure 11 shows  $\langle Tu \rangle_{yz}$ , and  $\langle (V,W) \rangle_{yz}$  versus  $N_{EHD}$  for non-staggered and staggered electrode emitters. For the non-staggered electrode both parameters increase with increasing values of  $N_{EHD}$ . This suggests the appearance of well-organized and stable secondary flows that just continue to increase in strength as the electric force acting on the gas increases relative to the axial flow inertia. The corresponding increase in turbulence intensity suggests that turbulence production is primarily associated with the shear flow of secondary flows and ‘corona wind’. For the staggered electrode, on the other hand,  $\langle Tu \rangle_{yz}$  is increasing but more slowly and the intensity of secondary flows is weak and only slowly increasing. It appears that the staggered arrangement of corona discharge emitters is less successful than the non-staggered arrangement in driving secondary flows in the form of axial rolls.

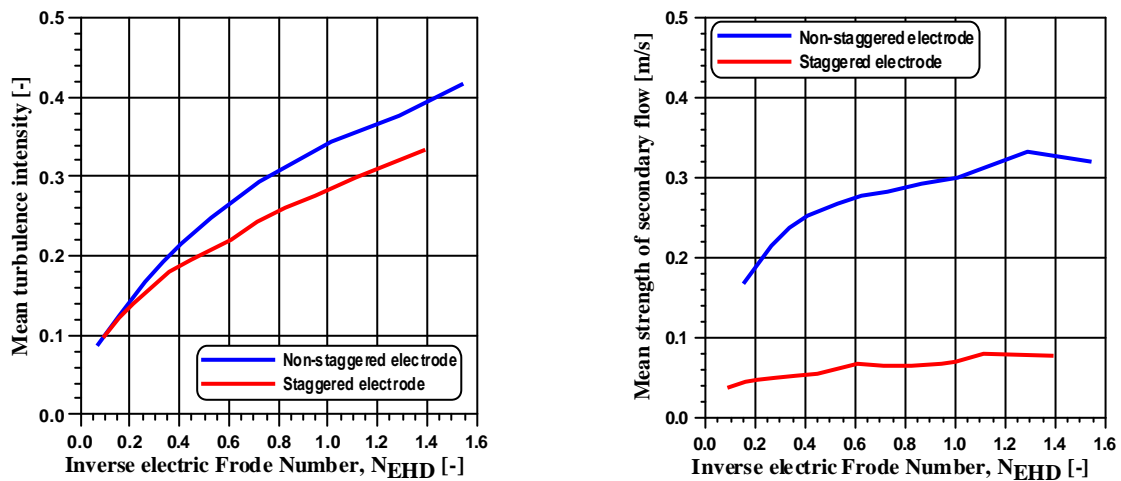


Figure 11. Computed values of mean turbulence intensity (left) and magnitude of mean secondary flow (right) versus inverse electric Frode number for non-staggered and staggered electrode emitters. Axial position: mid between 6<sup>th</sup> and 7<sup>th</sup> electrode.

Similar to Figure 10, for non-staggered and staggered electrodes, turbulence intensity and secondary flows but now for increasing values of  $N_{EHD}$  and fixed axial position mid between 6<sup>th</sup> and 7<sup>th</sup> electrode has been investigated (not shown). The study indicates increasing turbulence intensity with increasing  $N_{EHD}$  for both electrodes, as expected. Also the considerable difference in secondary roll

pattern between non-staggered and staggered electrodes was identified. But the secondary flow pattern was maintained for both electrode arrangements with increasing  $N_{EHD}$ .

### Parametric study of particle diffusivity coefficient

Figure 12 shows computed distributions and cross-sectional mean values of turbulent kinetic energy  $k$ , turbulent dissipation  $\epsilon$ , and normalized turbulent viscosity  $\nu_T/\nu$ , for non-staggered and staggered electrodes at the downstream reference case of  $N_{EHD} = 0.33$ . Differences in distributions reflect differences in secondary flows. Mean values of  $\nu_T/\nu$ , hence particle diffusivity coefficient  $D_T = (\nu_T/\nu)/\sigma$ ,  $\sigma = 0.9$  (see above), are of the same order of magnitude, although slightly greater for the staggered electrodes.

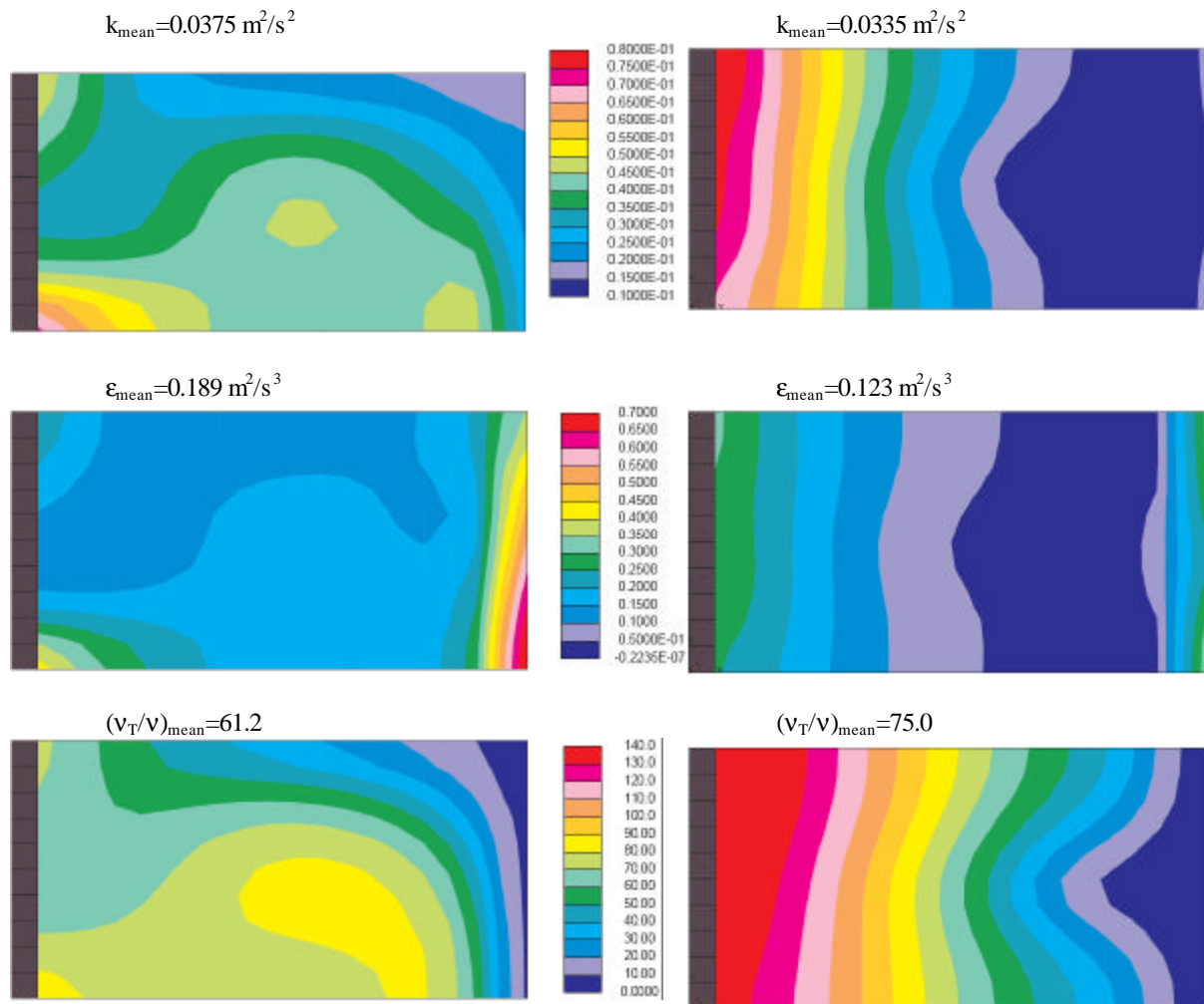


Figure 12. Computed turbulent kinetic energy (upper), turbulent dissipation (middle), and normalized turbulent viscosity (lower) for non-staggered (left) and staggered (right) electrode emitters. Axial position: mid between 6<sup>th</sup> and 7<sup>th</sup> electrode. Inverse electric Frode number:  $N_{EHD}=0.33$ .

Since  $D_T$  is a key parameter in calculating the efficiency of an ESP, it has been desirable to attempt to estimate values of  $D_T$  or  $\nu_T/\nu$  from the experimental stereo-PIV data. One approach is to use measured values of  $k$  and estimate the dissipation  $\epsilon$  from the longitudinal Taylor micro scale  $\lambda_f$  and then get  $\nu_T/\nu$ , according to the relations (Hinze, 1959)

$$\varepsilon = 30 v u_{\text{rms}}^2 / \lambda_f^2, \quad \lambda_f^2 = 2 \langle uu \rangle / \langle (\partial u / \partial x)^2 \rangle, \quad v_T / v = C_\mu k^2 / (v \varepsilon). \quad (3)$$

Here,  $u_{\text{rms}}^2 = \langle uu \rangle$ ,  $\langle \rangle$  denotes the average of all of 1000 vector maps where  $(\partial u / \partial x)^2$  is evaluated at each point of the vector map by second-order accurate spatial differentiation. Although results show considerable scatter, experimental values of  $v_T / v$  are found to be in the range of 50 to 100, which is in agreement with the computed values of Figure 12.

### Parametric study of efficiency

Figure 13 shows the computed efficiency for non-staggered electrodes to be slightly larger than for staggered electrodes for all values of  $N_{\text{EHD}}$ . According to the model study of Larsen and Sorensen (1984) one should expect increasing efficiency with decreasing values of diffusivity  $D_T$  and decreasing strength of secondary flows, both of which tend to increase the mixing and uniformity of concentration between discharge electrode and collector plate. According to Figure 12, computed values of  $v_T / v$ , being proportional to the values of  $D_T$  employed to calculate the particle transport and hence efficiency, do appear to be smallest for non-staggered electrodes. Hence, in agreement with the expected trend. However, the strength and regularity of secondary flows is by far the smallest for non-staggered electrodes, which contradicts the expected trend. Further calculations with the present model have shown lower efficiencies in the case of setting to zero the electric body force acting on the gas (zero secondary flow) for both non-staggered and staggered electrodes. Finally it is noted that quite low efficiencies are observed in Figure 13 which is lower than measured values. It is hypothesised that this discrepancy, which is only found for small size particles, is related to the turbulent, near-wall, coherent structures with fluctuations penetrating into the viscous dominated sublayer. Any of the above issues need further studies.

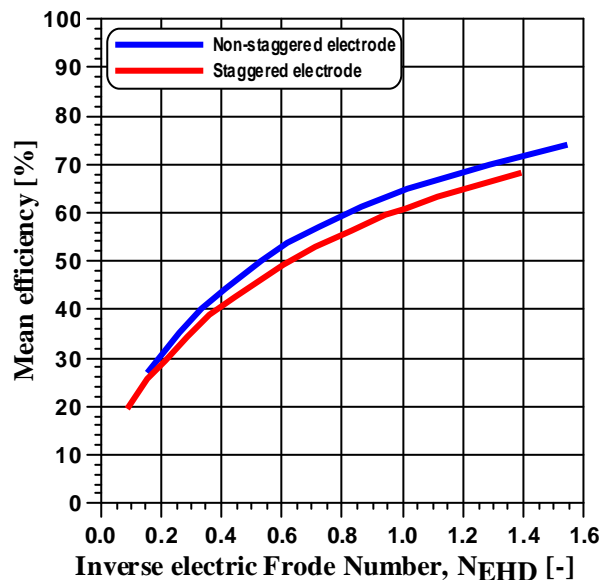


Figure 13. Computed values of mean efficiency versus inverse electric Frode number for non-staggered and staggered electrode emitters. Axial position at scale model outlet.

Recalling Figure 6, left, and corresponding text equally values of the defined quality criteria were found for non-staggered and staggered electrodes. But from Figure 13 the efficiency for the non-

staggered is larger than for the staggered electrode. Hence, it appears that there is no clear relation between current distribution at collector plate and efficiency.

## REFERENCES

- Akoh, E. & Nielsen, N.F., 2000, EFP-2000: *Electrostatic Precipitation – Reduction of Emission and Energy Consumption*, Software Specification, FORCE Technology (formerly DMI) report: TN.2000878, FORCE Technology, Lyngby, Denmark.
- Anagnostopoulos, J., Bergeles, G.C., 2002, *Corona discharge simulation in wire-duct electrostatic precipitator*, *J Electrostat*, **54**, p.129-147.
- Arrondel, V., Bacchiega, G., Gallimberti, I., 2001, *ESP Modelling: From University Studies to Industrial Application*, Proceedings of 8th. International Conference on Electrostatic Precipitation, May. 14-17, 2001, Birmingham, Alabama, USA, Session A4-2.
- Blanchard, D., Atten, P., Dumitran, L.M., 2002, *Correlation between current density and layer structure for fine particle deposition in a laboratory electrostatic precipitator*, *IEEE Trans. Ind. Applicat.*, **38**, p.832-839.
- Blanchard, D., Dumitran, L.M., Atten, P., 2001, *Electroaerodynamic secondary flow in an electrostatic precipitator and its influence of small diameter particles*, Proceedings of 8th. International Conference on Electrostatic Precipitation, May. 14-17, 2001, Birmingham, Alabama, USA, Session A2-1.
- Davidson, J.H., Shaughnessy, E.J., 1986, *Turbulence generation by electric body forces*, *Exp. Fluids*, **4**, p17-26.
- Egli, W. Kogelschatz, U. & Persson, T., 1996, *Three-Dimensional Corona Current Distribution in Complex ESP Configurations*, Proceedings of 6th. International Conference on Electrostatic Precipitation, June 18-21, 1996, Budapest, Hungary, pp.166-171.
- Ferziger, J. H. & Peric, M., 1996, *Computational Methods for Fluid Dynamics*, Springer.
- Gallimberti, I., 2004, *Detailed mass balance in electrostatic precipitators under industrial operating conditions*, Proceedings of 8th. International Conference on Electrostatic Precipitation, May. 17-21, 2004, Mpumalanga, South Africa, Invited lecture.
- Hinze, J.O., 1959, *Turbulence*, McGraw-Hill Book Co.
- Houlgreave, J.A., Bromley, K.S. & Fothergill, J.C., 1996, *A Finite Element Method for Modelling 3D Field and Current Distribution in Electrostatic Precipitators with Electrodes of Any Shape*, Proceedings of 6th. International Conference on Electrostatic Precipitation, June 18-21, 1996, Budapest, Hungary, pp.154-159.
- Larsen, P.S., Sørensen, S.K., 1984, *Effect of secondary flows and turbulence on electrostatic precipitator efficiency*, *Atmos. Environ.*, **18**, p1963-1967.
- Larsen, P.S., 1986, *Secondary flows in negative corona precipitator*, DCAMM report No. **337**, Techn. University of Denmark.
- Larsen, P.S., Poulsen, J.D., Pedersen, J.M., Meyer, K.E., Ullum, T., Nielsen, N.F., Lind, L., 2004, *Turbulence studies of negative corona ESP*, Proceedings of 8th. International Conference on Electrostatic Precipitation, May. 17-21, 2004, Mpumalanga, South Africa, Paper A05.
- Lauder, B.E., and Spalding, D.B., 1974, *The numerical computation of turbulent flow*, *Comp. Meth. in Appl. Mech. & Eng.*, **3**, p. 269.
- Lawless, P.A., 1996, *ESPM 4.0 Electrostatic Precipitator V-I Performance Model - User's Manual*. Center for Aerosol Technology, Research Triangle Institute, North Carolina, USA.

- Leonard, G., Mitchner, M., Self, S.A., 1980, *Particle transport in electrostatic precipitators*, Atmos. Environ., **14**, p1289-1299.
- Lind, L., Nielsen, N.F., Larsen, P.S., Hove, E.A., 2004, *Simulation of particle transport in electrostatic precipitators*, Proceedings of 8th. International Conference on Electrostatic Precipitation, May. 17-21, 2004, Mpumalanga, South Africa, Paper A24.
- Medlin, A.J., Fletcher, C.A.J. & Morrow, R., 1998, *Electrohydrodynamic Modelling of Fine Particle Collection in Electrostatic Precipitators*, Proceedings of 7th. International Conference on Electrostatic Precipitation, Sept. 20-25, 1998, Kyongju, Korea, pp.665-672.
- Meroth, A.M., Nicolaus, S., Levin, P.L. & Schwab, A.J., 1996, *Effective Solution of 3D Charge Coupled Problems in Electrostatic Precipitators*, Proceedings of 6th. International Conference on Electrostatic Precipitation, June 18-21, 1996, Budapest, Hungary, pp.137-143.
- Nielsen, N.F., Lind, L., 2004, *CFD simulation of gas flow and particle movement in ESPs*, Proceedings of 8th. International Conference on Electrostatic Precipitation, May. 17-21, 2004, Mpumalanga, South Africa, Paper A22.
- Parasram, N.R., Taylor, A.M.K.P., 2001, *Particle motion in electrostatic precipitators*, Proceedings of 8<sup>th</sup>, International Conference on Electrostatic Precipitation, May. 14-17, 2001, Birmingham, Alabama, USA, Session A1-2.
- Schmid, H.-J. & Buggisch, H., 1998, *On the Modelling of Particle Transport in Electrostatic Precipitators*, Proceedings of 7th. International Conference on Electrostatic Precipitation, Sept. 20-25, 1998, Kyongju, Korea, pp.673-687.
- Schmitz, W., Gibson, D. & Pretorius, L., 2001, *Computational Fluid Dynamics Modelling of Collection Dynamics*, Proceedings of 8th. International Conference on Electrostatic Precipitation, May. 14-17, 2001, Birmingham, Alabama, USA, Session A2-1.
- Soldati, A., 2003, *Cost/efficiency analysis of a wire-plate ESP with an advection diffusion equation for turbulent particle transport*, Aerosol Sci. and Technol., **37**, p171-182.
- STAR-CD manual, version 3.15, 2001, Computational Dynamics Ltd., London, UK.
- Thomsen HP; Larsen PS; Christensen EM; Christiansen JV, 1982, *Velocity and turbulence fields in negative corona wire-plate precipitator*. Fourth Symp. on the Transfer and Utilization of Particulate Control Technology, Houston, Texas, 1982 (II, p.243, EPA-600/9-025 b, Nov.1984).
- Ullum, T., Larsen, P.S., Özcan, O., 2004, *Three-dimensional flow and turbulence structure in electrostatic precipitator*, J. Exp. Fluids., **36**, p91-99.
- Ullum, T., Larsen, P.S., 2004, *Swirling flow structures in electrostatic precipitator*, Turbulence and Combustion, **73**, p259-275.
- Wilcox, D.C. 1993, *Turbulence Modeling for CFD*, DCW Industries, Inc., California, USA.
- Yamamoto, T., Velkoff, H.R., 1981, *Electrohydrodynamics in an electrostatic precipitator*, J. Fluid Mech., **109**, p1-18.
- Zamany, J., 1992, *Modelling of particle transport in Commercial Electrostatic Precipitators*, Ph.D Thesis, ATV EF 316, Technical University of Denmark and FLS Airtech A/S (formerly FLS miljø a/s).
- Zamany, J., 1995a, *Numerical modeling of electrodynamic conditions influenced by particle space charge and resistivity in electrostatic precipitators of complex geometry for industrial applications*, Inst Phys Conf Ser No **143**: 357-362.

Zamany, J., 1995b, *Numerical modeling of electrodynamic conditions influenced by particle space charge and resistivity in electrostatic precipitators of complex geometry for industrial applications*, FLS Airtech A/S (formerly FLS miljø ) Internal report, FLS Airtech, Valby, Denmark.